Inorg. Chem. **2005**, *44*, 9267–9278

Neutron Powder Diffraction Study of $Pb(Hf_xTi_{1-x})O_3$ Ceramics ($0.10 \leq x \leq 0.50$)

J. Frantti,*,†,⊥ Y. Fujioka,†,⊥ S. Eriksson,‡ S. Hull,§ and M. Kakihana||

Materials and Structures Laboratory, Tokyo Institute of Technology, 4259 Nagatsuta, Midori-ku, Yokohama, 226-8503, Japan, Studsvik Neutron Research Laboratory, Uppsala University, SE-611 82, Nyköping, Sweden, The ISIS Facility, Rutherford Appleton Laboratory, Chilton Didcot, Oxfordshire, OX11 0QX, U.K., and Institute of Multidisciplinary Research for Advanced Materials, Tohoku University, Sendai 980-8577, Japan

Received July 13, 2005

The crystal symmetries of lead hafnate titanate ($Pb(Hf_xTi_{1-x})O_3$, PHT) powders with $0.10 \leq x \leq 0.50$ were investigated by high-resolution neutron powder diffraction. Samples with $x \leq 0.40$ were tetragonal (space group *P*4*mm*), while the sample with $x = 0.50$ contained both monoclinic *Cm* and rhombohedral (modeled using the *R*3*c* space group) phases. The role of the B cations (Hf and Ti) and the oxygen octahedra network, in addition to the displacement of Pb ions from their ideal sites, in promoting the phase transformation between the *P*4*mm* and *Cm* phases was considered. Two types of structural disorder were identified. Diffuse scattering between Bragg reflection peaks was assigned to Pb ion displacement. A second type of structural disorder, revealed by the weak intensities of observed pseudo-cubic 00*l* reflections with *l* even and as 00*l* reflection peak widths significantly broader than the *l*00 reflection peaks, was observed. This behavior was attributed to disorder in the arrangement of the O–B–O rows parallel to the *c* axis. For small values of *x*, this shift was predominantly along the *c* axis, whereas shifts perpendicular to the *c* axis increased with increasing *x*. These features were modeled using an *hkl*-dependent line-broadening model. The origin of the *hkl*-dependent line broadening was assigned to the microstrain accompanying a spatial-composition variation. Structural models were tested by computing valence sums and spontaneous polarization values.

1. Introduction

Ferroelectric materials have numerous applications, which are based on electrostrictive, piezo-, pyro-, and ferroelectric phenomena. These applications include nonvolatile memory devices, infrared detectors, and actuators.[1] Oxide perovskites are commonly used for these applications. They have a rather simple crystal structure and can conveniently be prepared in the form of both bulk ceramics and thin films. Among the most widely used materials are lead zirconate titanate ($Pb(Zr_xTi_{1-x})O_3$, PZT) ceramics, where *x* is adjusted so that the desired property for a particular application (such as the electromechanical-coupling coefficient in piezoelectric applications or the pyroelectric coefficient for infrared detectors) is optimized. The spontaneous polarization vector, $\mathbf{P}_S$, has a central role, as the vast majority of the applications either measure (sensors) or generate (actuators and memory cells) changes in $\mathbf{P}_S$ with temperature, pressure, or electric field. Detailed analysis of the crystal structure and defects provide information concerning the magnitude, direction, and reversibility of $\mathbf{P}_S$. A polarization rotation mechanism was invoked to explain the unusually high piezoelectric coefficients of PZT with composition in the vicinity of the morphotropic phase boundary (MPB).[2,3] The MPB is traditionally understood to mean an almost constant line in *x*, which separates the rhombohedral and tetragonal phases, in the $x-T$ plane. A current opinion is that the concept of MPB should be understood as a "morphotropic phase" with *Cm* symmetry.[4] More recently, Raman scattering and neutron

* To whom correspondence should be addressed. E-mail: jfr@fyslab.hut.fi.
† Tokyo Institute of Technology.
‡ Uppsala University.
§ Rutherford Appleton Laboratory.
|| Tohoku University.
⊥ Present address: Laboratory of Physics, Helsinki University of Technology, P.O. Box 1100, FIN-02015 HUT, Finland.

(1) Lines, M. E.; Glass, A. M. *Principles and Applications of Ferroelectric and Related Materials*; Oxford University Press: Oxford, U.K., 2001.
(2) Noheda, B.; Cox, D. E.; Shirane, G.; Gonzalo, J. A.; Cross, L. E.; Park, S.-E. *Appl. Phys. Lett.* **1999**, *74*, 2059.
(3) Fu, H.; Cohen, R. E. *Nature* **2000**, *403*, 281.
(4) Noheda, B.; Gonzalo, J. A.; Cross, L. E.; Guo, R.; Park, S.-E.; Cox, D. E.; Shirane, G. *Phys. Rev. B* **2000**, *61*, 8687.

10.1021/ic051169m CCC: $30.25
Published on Web 11/01/2005

powder diffraction (NPD) techniques were used to investigate the response of PZT ceramics with increasing hydrostatic pressure.[5,6] The polarization was found to rotate toward the pseudocubic [111] direction with increasing pressure. This effect was accompanied by a series of phase transitions via monoclinic phases to triclinic ones. A crucial factor was that the symmetry of these new phases allowed octahedral tilting, which in turn allowed compression of the crystal particularly through the compression of the cuboctahedral cage surrounding the Pb ion (the relationships between the ratio of the octahedra and cuboctahedra volumes and octahedra tilts are given in ref 7). This behavior was analogous to the behavior occurring with decreasing temperature; the magnitude of $\mathbf{P}_S$ was decreasing with increasing hydrostatic pressure, whereas it was found to increase with decreasing temperature. It was concluded that the polarization rotation occurs with *x*, temperature, and pressure, and it was proposed that these materials can respond to the external field or pressure with ease because certain symmetries allow the polarization to be rotated without the need to change the symmetry (and to provide additional energy to cross the corresponding energy barrier).[2,5,6]

The polarization rotation explanation relies on average crystal symmetries. Recently, it has been reported that local deviations from the average symmetry have a central role for understanding the phase transition in the vicinity of the MPB.[8,9] Examples of these local deviations are ions which are not at their ideal positions (such as Pb ions displaced toward the pseudocubic [110] direction or B cations having different fractional coordinates). In particular, Pb ion displacements were revealed by numerous neutron, X-ray powder diffraction, and X-ray absorption fine-structure spectroscopy (XAFS) studies.[2,4,14,15,18,21,22] A second-order parameter model was developed to allow the existence of the monoclinic phase (*Cm*) as a solution of the sixth order Devonshire theory.[8] Conventional Devonshire theory necessitates an eighth order model to allow a monoclinic phase to be a solution. Within this scheme, the local deviations from the average symmetry (*P*4*mm* or *R*3*m*) were taken to cancel out over a larger spatial scale (on the order of few hundred nanometers). For example, in the case of *P*4*mm* symmetry, the Pb ions are commonly assumed to be displaced with equal probabilities into four equivalent directions, which means that the only remaining macroscopic polarization (order parameter) component is along the tetragonal *c* axis direction. The second-order parameter model had two nonzero-order parameters only in the case of the *Cm* phase.[8] The phase transition between the *P*4*mm* and *Cm* phases was considered to be similar to the order−disorder phase transition. Within this scheme, the ordering was mainly related to the Pb ion displacement: in the *Cm* phase, the Pb ion displacements are all toward the pseudocubic [110] direction, whereas they are toward four ⟨110⟩ directions in the *P*4*mm* phase. Later, a similar idea was extended so that also the local structures of the *R*3*m* and *P*4*mm* phases were considered to be monoclinic.[9] Consequently, it was pointed out that there need not be any discrete phase boundaries across the MPB: the monoclinic phase was considered to correspond to those composition and temperature values for which the local regions had grown sufficiently that diffraction techniques see a distinct phase of *Cm* symmetry. This is an interesting possibility to consider. It should be noted that the situation is different for other phase boundaries in the PZT system. Although there is a generic agreement that Pb ions are displaced from their ideal positions and the local structure can be assigned to be monoclinic (as far as the Pb ion displacements are considered), the concept of phase boundary is useful once the two-phase "coexistence" observed within MPB region is considered.

Even though the Pb ions are displaced toward pseudocubic ⟨110⟩ directions inside the cuboctahedral cages, there seems to be abrupt changes in the oxygen network versus composition, temperature, or pressure. Raman scattering probes structural features down to the nanometer scale and is well suited for studies of local structures. It was found that the oxygen network abruptly changes once the composition changes from $x = 0.40$ to $x = 0.50$ in a case of PZT ceramics[11,12,13] and lead hafnate titanate, $Pb(Hf_xTi_{1-x})O_3$ (PHT), ceramics.[10] This change in the oxygen network was seen in the abrupt frequency jump of the B_1 mode, which only involves motion of the oxygen ions. In addition, Raman scattering revealed a well-resolved peak splitting which was not consistent with *P*4*mm* symmetry. Basically, this splitting supports the idea of a local monoclinic distortion. However, one should also assume that (i) the distortions (i.e., bond length distribution) within different monoclinic regions are almost identical (otherwise, the peak split would not be well resolved but would have the form of broad smeared peaks) and that (ii) the role of heavy Pb ions should be dominate in

(5) Rouquette, J.; Haines, J.; Bornand, V.; Pintard, M.; Papet, Ph.; Bousquet, C.; Konczewicz, L.; Gorelli, F A.; Hull, S. *Phys. Rev. B* **2004**, *70*, 014108.
(6) Rouquette, J.; Haines, J.; Bornand, V.; Pintard, M.; Papet, Ph.; Marshall, W G.; Hull, S. *Phys. Rev. B* **2005**, *71*, 024112.
(7) Thomas, N. W.; Beitollahi, A. *Acta Crystallogr., Sect. B* **1994**, *50*, 549.
(8) Bell, J. B.; Furman, E. *Jpn. J. Appl. Phys.* **2003**, *42*, 7418.
(9) Glazer, A. M.; Thomas, P. A.; Baba-Kishi, K. Z.; Pang, G. K. H.; Tai, C. W. *Phys. Rev. B* **2004**, *70*, 184123.
(10) (a) Frantti, J.; Fujioka, Y.; Eriksson, S.; Lantto, V.; Kakihana, M. *J. Electroceram.* **2004**, *13*, 299. (b) Frantti, J. *Phys. Rev. B* **1999**, *71*, 12.
(11) (a) Frantti, J.; Lantto, V.; Nishio, S.; Kakihana, M. *Phys. Rev. B* **1999**, *59*, 12. (b) Frantti, J.; Lappalainen, J.; Lantto, V.; Nishio, S.; Kakihana, M. *Jpn. J. Appl. Phys.* **1999**, *38*, 5679.
(12) Frantti, J.; Eriksson, S.; Hull, S.; Lantto, V.; Rundlöf, H.; Kakihana, M. *J. Phys.: Condens. Matter* **2003**, *15*, 6031.
(13) Souza Filho, A. G.; Lima, K. C. V.; Ayala, A. P.; Guedes, I.; Freire, P. T. C.; Mendes Filho, J.; Araújo, E. B.; Eiras, J. A. *Phys. Rev. B* **2000**, *61*, 14283.
(14) Muller, C.; Baudour, J.-L.; Madigou, V.; Bouree, F.; Kiat, J.-M.; Favotto, C.; Roubin, M. *Acta Crystallogr. B* **1999**, *55*, 8.
(15) Muller, C.; Baudour, J.-L.; Bedoya, C.; Bouree, F.; Soubeyroux, J.-L.; Roubin, M. *Acta Crystallogr. B* **2000**, *56*, 27.
(16) Shirane, G.; Pepinsky, R. *Phys. Rev.* **1953**, *91*, 812.
(17) *Handbook of Chemistry and Physics*; CRC Press: Boca Raton, FL, 1999.
(18) Frantti, J.; Ivanov, S.; Eriksson, S.; Rundlöf, H.; Lantto, V.; Lappalainen J.; Kakihana, M. *Phys. Rev. B* **2002**, *66*, 064108.
(19) Leineweber, A.; Mittemeijer, E. J. *J. Appl. Crystallogr.* **2004**, *37*, 123.
(20) Thompson, P.; Cox, D. E.; Hasting, J. B. *J. Appl. Crystallogr.* **1987**, *20*, 79.
(21) Corker, D. L.; Glazer, A. M.; Whatmore, R. W.; Stallard, A.; Fauth, F. *J. Phys.: Condens. Matter* **1998**, *10*, 6251.
(22) Sicron, N.; Yacoby, Y. *J. Synchrotron Rad.* **1999**, *6*, 503.

the case of the lowest-frequency modes. The experimental observation was that not only were the lowest-frequency modes split but also the mode at around 500 cm^{-1} (assigned to the splitting of the *E*(3TO) mode) was split. We note that although the Pb ion displacements in the *P*4*mm* phase can be taken as monoclinic, the same is not true with the oxygen octahedra (since the refinements of NPD data yielded very reasonable values for the oxygen positions and displacement parameters there was no reason to introduce a monoclinic distortion to the oxygen octahedra). As the oxygen ions have a crucial role for the vibrational spectra, an alternative model, relying on the anti-phase motion of Ti and Zr (PZT) or Ti and Hf (PHT) ions was proposed to explain the observed peak splitting.[10]

The previously reported models have focused on the role of Pb ions, with fewer studies considering the role of the B cations or oxygen octahedra network. The present study concentrates on the structural analysis of PHT powders, whose room-temperature symmetry was previously reported to be *P*4*mm* for Ti-rich concentrations.[14] A symmetry change to a rhombohedral form (space group *R*3*m*) occurs at $x \approx 0.50$. At higher hafnium content a further symmetry change occurs to the rhombohedral *R*3*c* phase.[15] The symmetry of $PbHfO_3$ is orthorhombic *Pbam*.[16] All phases, except the orthorhombic one (which is antiferroelectric), are ferroelectric. These features are similar to those found in PZT ceramics and are consistent with ionic radii considerations: 6-fold coordinated Hf^{4+} and Zr^{4+} have almost identical ionic radii, 0.78 and 0.79 Å, respectively.[17] However, the mass difference between these two ions is large, and one may expect it to have an effect on the vibrational properties. The vibrational entropy is one factor determining which phase is stable and the first purpose of this work was to reinvestigate the symmetries of the samples with $0.10 \leq x \leq 0.50$ and clarify the nature of the phase transition reported in ref 10. As the structures of both PHT and PZT ceramics may involve oxygen octahedra tilts, the neutron powder diffraction technique was used. For full structural characterization, the line shapes contain invaluable information. The second topic in this study is related to the crystal defects. In addition to the Bragg peak positions and intensities, the *hkl*-dependent line broadening contains interesting information concerning crystal defects. In practice, one can extract such information using a high-resolution neutron powder diffractometer, such as the HRPD instrument at ISIS. In the case of PHT- and PZT-type solid solutions, spatial composition variations result in *hkl*-dependent line broadening, which was demonstrated in the case of PZT powder with $x = 0.54$.[12] It has also been customary to assign diffuse scattering, seen most clearly between the tetragonal 200 and 002 reflections, to Pb ions disordered over the four sites about the *c* axis. This is also a topic we address. Profile function selection is crucial to extract correct structural data from Rietveld refinements. The third goal was to provide accurate structural data for the computational studies of the phase stabilities of PHT and PZT ceramics versus *x* and temperature.

2. Experimental Section

2.1. Sample Preparation. Lead hafnate titanate Pb(Hf$_x$Ti$_{1-x}$)O$_3$ powders with $0.10 \leq x \leq 0.50$ were prepared using the solid-state reaction technique. PbO, HfO_2, and TiO_2 powders were weighed in the desired composition ratios. After the powders were mixed by ball milling with ethanol, the samples were pressed into pellet form and annealed at 800 °C for 1 h; after which pellets were ground and ball milled again. The resulting powders were pressed into pellet form and sintered at 1100 °C for 1 h. Finally, the pellets were ground for the powder diffraction experiments. During annealing and sintering PHT, the pellets were under an inverted alumina crucible (sealed with alumina powder). The pellets were covered by the same PHT powder that was used for the preparation of the pellet. The purpose of this procedure was to ensure that the PbO loss is not significant (the vapor pressure of Hf and Ti oxides is neglible when compared to the vapor pressure of PbO). Phase purity was confirmed by X-ray powder diffraction experiments. All samples, except the $x = 0.50$ sample, were single-phase samples. As in the case of PZT, there is a phase boundary at around $x = 0.50$ which leads to a two-phase coexistence because of the spatial variation of *x*.[24]

2.2. Neutron Powder Diffraction Data Collection. Time-of-flight (TOF) neutron powder diffraction data were collected using the high-resolution powder diffractometer (HRPD) instrument at the Rutherford Appleton Laboratory, ISIS, UK. In the case of the tetragonal samples, data were collected at room temperature and at 4 K. In the case of the $x = 0.50$ sample, data were collected at 2, 50, 140, and at 280 K. A helium cryostat was used for the low-temperature measurements. The backscattering data bank (No. 1, which contains the highest resolution data) was used in this study, although the data collected on other banks were investigated for confirmation of space group assignments. The instrumental parameters (σ_1, α, β_0, and β_1, to be described below) were determined by the beamline scientists at ISIS using standard calibration samples. Since the data on the $x = 0.50$ sample were collected at different times than the data for the other samples, the instrument parameters also are slightly different.

2.3. Refinement Models. 2.3.1. Profile Function. All Rietveld refinements were carried out using the general structure analysis system (GSAS).[25] As there was clear evidence of reflection index dependent line broadening, the TOF profile function No. 4, which is a phenomenological description for the *hkl*-dependent (microstrain) broadening due to Stephens[26] was used. In the case of the HRPD instrument, the sample imperfections are almost completely responsible for the observed line broadening. The diffraction line broadening from the lattice-parameter variations caused by a spatial scalar variable, such as the composition, was recently analyzed theoretically and demonstrated experimentally by Leineweber and Mittemeijer.[19] They showed that redundant fit parameters occur in the Stephens description if the line broadening has its origin in one spatially varying scalar variable (such as composition or temperature). However, this line shape is not yet implemented within current Rietveld programs. The use of constraints does not work in this case, as one should use square root-type relations between parameters, which are not available in Rietveld refinement

(23) Massa, W. *Crystal Structure Determination*; Springer-Verlag: Berlin Heidelberg, 2000.
(24) Jaffe, B.; Roth, R. S.; Marzullo, S. *J. Res. Natl. Bur. Stand.* **1955**, *55*, 239.
(25) Larson, A. C.; Von Dreele, R. B. *General Structure Analysis System, LANSCE MS−H805*; Los Alamos National Laboratory: Los Alamos, NM, 2000.
(26) Stephens, P. W. *J. Appl. Crystallogr*. **1999**, *32*, 281.

softwares. The GSAS TOF profile function 4 is a result of a convolution between a pair of back-to-back exponentials (characterized by the α, β_0, and β_1 parameters) and a pseudo-Voigt function. Thus, this profile function has Gaussian and Lorentzian contributions to the line broadening. The Gaussian contribution is $\sigma^2 = \sigma_1^2 d^2 + \sigma_2^2 d^4 + \sigma_S^2 d^6$ and the Lorentzian contribution is $\gamma = \gamma_2 d^2 + \gamma_{2e} d^2 \cos\phi + \gamma_S d^3$, where σ_1 is in microseconds per angstrom, σ_2, γ_2, and γ_{2e} are in microseconds per square angstrom, and σ_S and γ_S are in microseconds per cubic angstrom. The instrumental contribution is mainly Gaussian. In the present case, $\sigma_1^2 = 225$ μs^2 Å^{-2} (except for the $x = 0.50$ sample, for which $\sigma_1^2 = 209.1$ μs^2 Å^{-2}). Although the strain broadening contributes to σ_1, we did not refine it (trials were carried out, but σ_1 tended to diminish to zero). The linebroadening from the sample (most notably the result of the strain and particle size effects) is often predominantly Lorentzian. In addition, γ_2 and γ_{2e} were fixed at zero (they describe the isotropic and anisotropic strain broadening, respectively). The ϕ is the angle between the broadening axis, determined as a part of the refinement model, and the *hkl* plane. The *hkl*-dependent line broadening is taken into account by microstrain broadening terms, Γ_S, which for the Laue symmetries 4/*mmm* and 2/*m*, are written as $\Gamma_S^2 = S_{400}(h^4 + k^4) + S_{004}l^4 + 3S_{220}h^2k^2 + 3S_{202}(h^2l^2 + k^2l^2)$ and $\Gamma_S^2 = S_{400}h^4 + S_{040}k^4 + S_{004}l^4 + 3S_{202}h^2l^2 + 3(S_{220}h^2k^2 + S_{022}k^2l^2) + 2(S_{301}h^3l + S_{103}hl^3) + 4S_{121}hk^2l$, respectively ($\Gamma_S^2$ for other symmetries are given in refs 25 and 26). The microstrain is divided into Gaussian and Lorentzian parts by introducing a mixing coefficient η: $\gamma_S = \eta\Gamma_S$ and $\sigma_S = (1 - \eta)\Gamma_S$. Although the peak widths are computed numerically in GSAS, an approximation for the full-width-at-half-maximum (fwhm) Γ can be obtained from the equation[20]

$$\Gamma = (\Gamma_g^5 + 2.69269\Gamma_g^4\gamma + 2.42843\Gamma_g^3\gamma^2 + 4.47163\Gamma_g^2\gamma^3 + 0.07842\Gamma_g\gamma^4 + \gamma^5)^{1/5} \quad (1)$$

The Gaussian fwhm, Γ_g, is $\sqrt{(8\ln 2)\sigma^2}$. This equation is valid for the pseudo-Voigt function, and in practice, small differences in the observed fwhm are found because the profile function has contributions from the aforementioned exponential functions. Our purpose was to use this equation to extract the instrument-independent broadening by substituting only microstrain parameters.

2.3.2. Structural Model. In the case of PZT and PHT solid solutions, the B cation sites are statistically occupied by two cation species, but their fractional coordinates are not the same, as was reported in refs 14, 15, 18, 21, and 22. This type of disorder means that there are often difficulties when refining the B cation positions, occupancies, absorption coefficients, and displacement parameters reliably, as they tend to be correlated. The correlation between the occupancies and displacement parameters is somewhat pronounced in the case of the HRPD instrument because a neutron guide must be used to obtain a high resolution. This in turn results in a weaker quality data at short *d* spacings, which contain invaluable information from displacement parameters. In the case of PZT and PHT solid solutions, negative displacement parameters can be a sign of problems with occupancies (for example, the fraction of heavy atoms, Zr or Hf, is larger than assumed), an incorrect account of absorption effects, that the constraint that different ions share the same fractional coordinates is not reasonable, or a poorly refined background. Useful information can often be gained by studying the anisotropic displacement factors. If certain diagonal components are negative, it might be an indication that the corresponding fractional coordinates of different ions differ. In such a case, one may adopt the so-called split-atom model.[23] It is also known that Pb ions tend to be displaced from their ideal site. This is observed experimentally as an abnormally large Pb ion displacement parameter. A better fit can often be achieved either by using anisotropic displacement parameters or by placing Pb ions on a lower-symmetry position. We note that if the fractional coordinates of the B cations are allowed to be different, it might be better to place the Pb ions in a lower-symmetry position and not use anisotropic displacement parameters.

More reliable refinements can be obtained once other methods are used to estimate the composition and the effect of absorption. Thus, wavelength-dispersive spectroscopy and energy-dispersive spectroscopy of X-rays were used to study the average compositions of the samples. Composition analysis confirmed that the average composition (within the micrometer scale, which was the spatial resolution) was very close to the nominal one. Correspondingly, occupancies were not refined for the single-phase (tetragonal) samples. However, occupancies were refined in the case of the $x = 0.50$ sample. Although the average composition for this sample was close to the nominal one, it is appropriate to refine the occupancies for this sample as it contained two phases. This is the result of spatial composition variation, which, in the case of PZT ceramics, is discussed in ref 12. After a good fit of the atomic positions, profile, lattice, and background parameters was obtained, an overall isotropic displacement parameter was refined (occupancies were fixed to their nominal values), after which it was fixed and the occupancies were refined. In the following refinement stage the occupancies were fixed, and the individual isotropic displacement parameters were refined. An attempt to refine all parameters simultaneously resulted in divergent refinement, related to the aforementioned correlation issue. Correspondingly, no standard errors are given for the occupancies.

Second, absorption corrections were carried out for each sample by measuring the sample mass, volume, and sample container diameter. These figures, together with the tabulated neutron absorption and scattering cross sections, allowed us to apply absorption corrections prior to the refinement procedure. All temperature factors were refined for each ionic species, except in the case of the $x = 0.30$ sample. For this sample, the B cation displacement parameters turned out to be negative. Thus, we decided to use a common displacement parameter for all cations. The mass of this sample was smaller than the mass of the other samples. Even though a considerably longer measurement time was used to gain sufficient counting statistics, the problem with the displacement parameters was evident. In addition, in the case of the tetragonal ($0.10 \le x \le 0.40$) samples, it was necessary to allow a refinement of individual fractional *z* coordinates for Hf and Ti. The physical background for this is given below. A linear interpolation function (seven terms) was used to model the background contribution.

3. Results

3.1. Structural Data. Figure 1 shows the time-of-flight (TOF) data collected on PHT samples with $0.10 \le x \le 0.50$ at 4 K. Except for the $x = 0.50$ sample, data were modeled using *P*4*mm* symmetry. Tables 1 and 2 give the structural parameters for the tetragonal samples and $x = 0.50$ sample, respectively. The data collected on the $x = 0.50$ sample was modeled using two phases. The major phase had monoclinic *Cm* symmetry. Although the refinement containing only this phase was almost acceptable, a second rhombohedral phase with symmetry *R*3*c* was also included because some weak but observable peaks were present, specifically at *d* spacings of around 1.06, 1.37, and 1.85 Å. These peaks could be

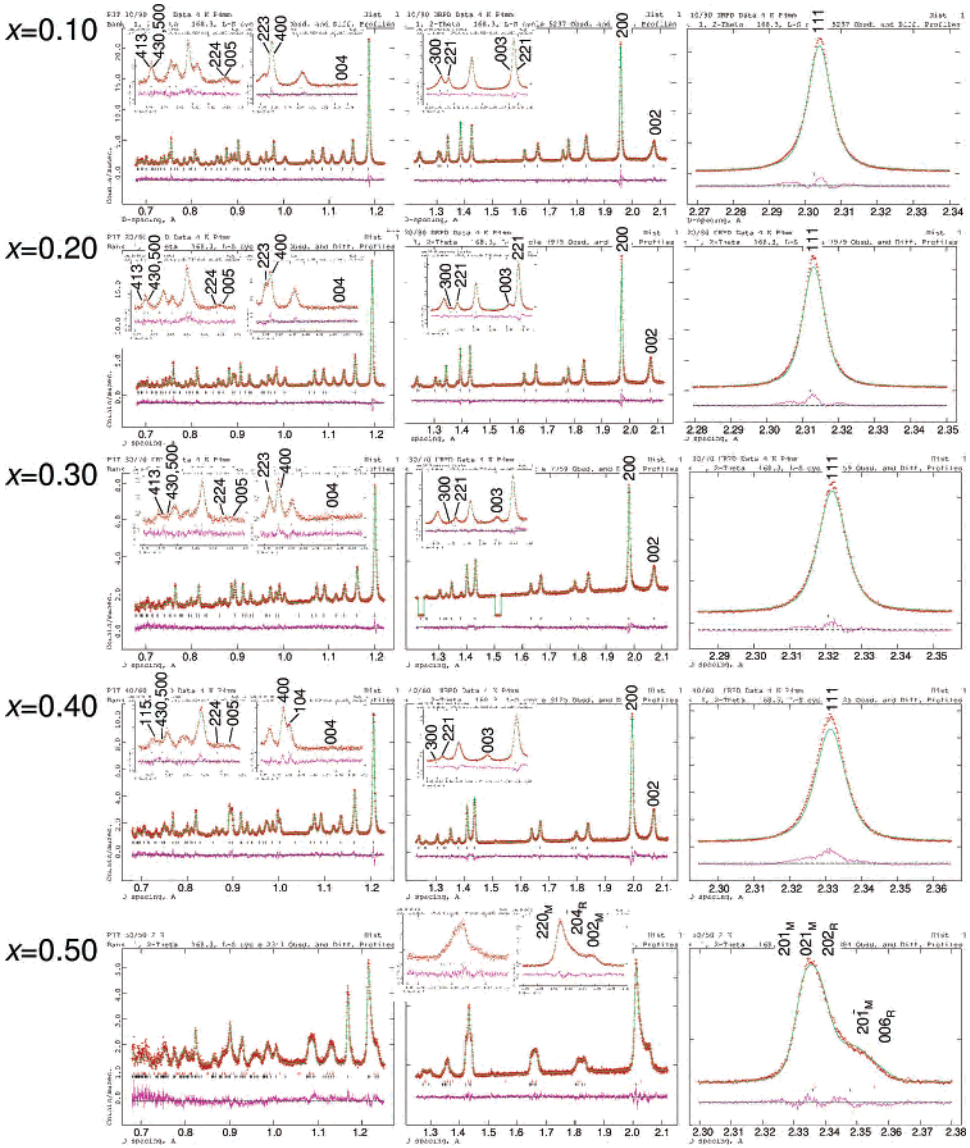

Figure 1. Observed and calculated TOF profiles and the corresponding difference curves for tetragonal PHT samples with 0.10 ≤ x ≤ 0.40 at 4 K and for the x = 0.50 sample at 2 K. In the case of the four uppermost rows, the tick marks correspond to the Bragg reflections from the *P*4*mm* phase. Insets show the *h*00 and 00*l* reflections enlarged. Overlapping reflections are indicated. Note the significant broadening of the 002 reflections when compared to the 200 reflections. The diffraction pattern revealed that the x = 0.50 sample contained two phases (see text). The major phase was modeled using *Cm* symmetry (lower tick marks) and the secondary phase was modeled using *R*3*c* symmetry (upper tick marks). In the case of the x = 0.50 data, labels R and M are used to indicate reflections which were characteristic of the *R*3*c* and *Cm* phases, respectively. Insets in the bottom row can be compared with Figure 2.

indexed using *R*3*c* symmetry (the highest symmetry able to explain the observed features). Also the region between 2.0 and 2.1 Å revealed that the diffraction pattern cannot satisfactorily be refined using only a single phase. As in the case of PZT with 0.52 ≤ x ≤ 0.54, two peaks (corresponding to the pseudo-cubic 200 and 002 reflections) were not sufficient for a good refinement.[12,18] This is consistent with the fact that both PZT and PHT become rhombohedral at large values of x, although the PZT sample with x = 0.50 did not show traces from the second phase.[4,18] This implies that at 2 K the phase boundary of the PHT system is located slightly below x = 0.50. In addition, it was crucial to use the correct line shape for both symmetries, since the pseudo-cubic 200 reflections have rather strong intensities.[27] The weight fraction of the rhombohedral phase was estimated to be 25%, see Table 2. Although the structural parameters for the rhombohedral phase must be treated with some caution, the values extracted from the 2 K data are reasonable. The occupancies for this phase (especially for Hf and Ti) were strongly dependent on temperature, and they probably reflect the problems related to disorder at the B cation site (the phase boundary between the rhombohedral and tetragonal regions, in the $x-T$ plane, may not be vertical implying that at higher temperatures only those crystals with the largest amount of Hf are rhombohedrally distorted; however, the present data do not address this problem). It is also well-known that Pb ions tend to be displaced from their ideal positions (e.g., in the case of *P*4*mm* symmetry Pb ions typically shift from the Wyckoff special position 2*a* into a general position; similar

(27) Correspondingly, the refinement emphasizes this region. Thus, if insufficient (say, symmetrical instead of asymmetrical) line shape is used for either phase, the fit of the weaker Bragg reflection peaks becomes worse (typically, superlattice reflections are weak and are less highly weighted in the refinements). This in turn may result in erroneous structural data or even an incorrect symmetry assignment.

Table 1. Structural Data and Statistical Figures of Merit for the $0.10 \le x \le 0.40$ Samples[a]

x	0.10	0.10	0.20	0.20	0.30	0.30	0.40	0.40
T (K)	4	295	4	295	4	295	4	295
a (Å)	3.915694(13)	3.926145(14)	3.940036(14)	3.950840(14)	3.963804(19)	3.976210(20)	3.988407(21)	4.001163(21)
c (Å)	4.150077(41)	4.131999(39)	4.146222(38)	4.124540(34)	4.141551(54)	4.118056(46)	4.139537(51)	4.115918(47)
U_{iso}(Pb) (Å^2)	0.00220(17)	0.00996(22)	0.00473(32)	0.0143(39)	0.00288(41)	0.01638(52)	0.00144(39)	0.01825(57)
U_{iso}(Ti,Hf) (Å^2)	0.00327(49)	0.00670(51)	0.0034(13)	0.0061(13)	0.00288(41)	0.01638(52)	0.0139(19)	0.0188(15)
U_{iso}(O_1) (Å^2)	0.01022(26)	0.01308(27)	0.01564(33)	0.01678(34)	0.01582(43)	0.02052(47)	0.01376(41)	0.02326(54)
U_{iso}($O_{2,3}$) (Å^2)	0.00741(15)	0.01214(17)	0.01217(23)	0.01553(24)	0.01089(32)	0.02063(37)	0.01577(37)	0.02451(42)
x(Pb)	0.01718(44)	0.02084(43)	0.02188(57)	0.02196(65)	0.02415(63)	0.02768(64)	0.02778(49)	0.02741(65)
z(Pb)	0.00000(33)	0.00000(34)	0.000(11)	0.000(10)	0.0000(64)	0.0000(36)	0.0000(76)	0.00000(0)
z(Hf)	0.5552(15)	0.5400(16)	0.5473(87)	0.5363(77)	0.56707(55)	0.54977(56)	0.5618(29)	0.57448(48)
z(Ti)	0.5441	0.5359	0.5430	0.5316	0.55688	0.53709	0.5490	0.57399
z(O_1)	0.11178(37)	0.10415(38)	0.108(11)	0.099(10)	0.10421(65)	0.0931(43)	0.0983(75)	0.08757(47)
z($O_{2,3}$)	0.62215(34)	0.61149(35)	0.621(11)	0.610(10)	0.6196(65)	0.6068(42)	0.6177(75)	0.60298(37)
χ^{2b}	3.247	2.700	2.992	2.530	2.405	2.291	3.416	3.042
R_{wp}(%)[b]	5.85	8.08	5.53	8.64	3.76	8.31	6.07	9.39
R_{wpb}(%)[b]	5.48	7.26	5.53	7.75	3.77	7.45	6.58	9.73
R_p(%)[b]	5.24	6.99	5.06	7.92	3.57	7.83	5.77	9.49
R_{pb}(%)[b]	4.87	6.27	5.17	7.38	3.66	7.39	6.59	10.18

[a] The space group was $P4mm$ for all samples, and during the refinements, the Ti ion position was kept fixed. In the case of the $x = 0.30$ sample, the temperature displacement parameters of all cations were fixed to be the same. See the text for details. [b] $\chi^2 = M_p/(N_{obs} - N_{var})$, $R_{wp} = \sqrt{M_p/\sum wI_o^2}$, $R_p = \sum|I_o - I_c|/\sum I_o$, $R_{wpb} = \sqrt{\sum w((I_o-I_c)(I_o-I_b)/I_o)^2/\sum w(I_o-I_b)^2}$, $R_{pb} = \sum(|I_o - I_c||I_o - I_b|/I_o)/\sum|I_o - I_b|$, where $M_p = \sum w(I_o - I_c)^2$, N_{obs} is the total number of observations, N_{var} is the number of variables in the refinement, w are the weights, I_o and I_c are the observed and calculated intensities, respectively, and I_b is the background contribution to the profile, see pages 165−167 of ref 25.

Table 2. Structural Data and Statistical Figures of Merit for the $x = 0.50$ Sample[a]

T (K)	2	2	50	50	140	140	280	280
space group	Cm	$R3c$	Cm	$R3c$	Cm	$R3c$	Cm	$R3c$
a (Å)	5.69565(19)	5.71961(23)	5.69674(18)	5.72018(22)	5.69881(22)	5.72243(23)	5.70117(19)	5.72501(19)
b (Å)	5.68281(15)		5.68365(15)		5.68721(18)		5.69188(17)	
c (Å)	4.10751(17)	14.13773(97)	4.10685(16)	14.13720(94)	4.10616(18)	14.13730(96)	4.10443(16)	14.13143(89)
β (deg)	90.436(2)		90.430(2)		90.389(2)		90.323(2)	
U_{iso}(Pb) (Å^2)	0.00761(65)	0.0046(12)	0.00715(62)	0.0038(12)	0.00980(83)	0.0058(15)	0.01241(89)	0.0112(17)
U_{iso}(Ti,Hf) (Å^2)	0.0055(13)	0.0105(31)	0.0044(12)	0.0091(28)	0.0083(16)	0.0072(26)	0.0098(15)	0.0121(25)
U_{iso}(O_1) (Å^2)	0.01066(89)		0.00964(82)		0.0119(11)		0.0146(11)	
U_{iso}($O_{2,3}$) (Å^2)	0.00968(64)	0.0061(11)	0.00897(59)	0.0049(10)	0.01091(75)	0.0054(12)	0.01329(76)	0.0083(11)
F(Pb)	0.974	0.985	0.967	0.967	0.954	0.977	0.933	0.963
F(Hf)	0.505	0.548	0.507	0.553	0.505	0.583	0.505	0.587
F(Ti)	0.495	0.452	0.493	0.447	0.495	0.417	0.495	0.413
F(O_1)	0.983		0.998		1.003		1.012	
F($O_{2,3}$)	1.036	1.000	1.035	1.012	1.049	0.999	1.063	1.008
z(Pb)		0.2739(11)		0.2739(10)		0.2739(10)		0.27193(99)
x(Hf/Ti)	0.4756(19)		0.4735(17)		0.4756(24)		0.4806(26)	
z(Hf/Ti)	0.5629(18)		0.5620(17)		0.5593(22)		0.5575(21)	
x(O_1)	0.46220(81)		0.46180(74)		0.46513(95)		0.4701(10)	
z(O_1)	0.08885(93)		0.08850(85)		0.0879(11)		0.0842(11)	
x($O_{2,3}$)	0.21929(63)	0.15338(78)	0.21876(59)	0.15483(71)	0.22113(77)	0.15934(95)	0.22583(80)	0.1635(12)
y($O_{2,3}$)	0.24911(59)	0.34794(85)	0.24890(54)	0.34780(77)	0.24930(72)	0.34654(91)	0.24977(79)	0.34513(85)
z($O_{2,3}$)	0.61026(70)	0.0725(12)	0.60921(66)	0.0724(11)	0.60718(82)	0.0741(12)	0.60300(80)	0.0730(12)
weight fraction	0.7536(5)	0.2464(47)	0.7572(5)	0.2428(44)	0.7416(6)	0.2584(51)	0.7260(57)	0.2740(47)
χ^2	2.213		2.295		1.746		1.973	
R_{wp}(%)	5.99		5.99		7.16		6.53	
R_{wpb}(%)	5.17		5.26		5.90		5.50	
R_p(%)	5.30		5.00		6.22		5.74	
R_{pb}(%)	4.98		4.70		5.58		5.26	

[a] This sample contained two phases, which were modeled by space groups Cm and $R3c$. During the refinements, either the Pb ions (space group Cm) or the Hf/Ti ions (space group $R3c$) were fixed at the origin. Occupancies are represented by F.

behavior is also observed in other symmetries), which explains the decreasing Pb occupancy with increasing temperature. The most important feature shown by this analysis is that the symmetry of the major phase decreases from $P4mm$ to Cm once x changes from 0.40 to 0.50. This confirms our Raman observation.[10] A model in which the main phase had $P4mm$ symmetry, instead of the Cm symmetry, was not satisfactory, see Figure 2. This was most clearly revealed by the large residuals of the peak and shoulder at around 2.0 and 2.3 Å (pseudocubic 200 and 111 reflections), although problems were also observed in other d spacing regions.

Although the main structural features were similar to the case of PZT ceramics reported in ref 18, there were clear differences at a finer scale. For the same value of x, the c axis length in PHT ceramics was smaller than that of PZT ceramics, while the a axis length was almost identical, as shown in Figure 3. Thus, the primitive cell volume of PHT ceramics was smaller than that of PZT ceramics. Also the 00l reflections were considerably broader than the h00

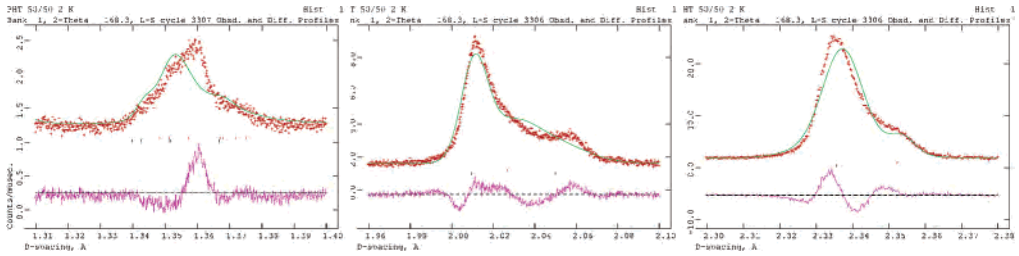

Figure 2. Rietveld refinement results for the $x = 0.50$ sample (data are the same as shown in Figure 1) using a model where the major phase had *P*4*mm* symmetry and the minor phase had *R*3*c* symmetry. The *d* spacing ranges corresponding to the pseudocubic (300), (200), and (111) reflections are shown. As is seen by comparing the fit above with the one shown in Figure 1, markedly smaller residuals were obtained using the *Cm* phase as the major phase. This was also seen from the goodness-of-fit parameters, which were significantly larger in the case of the *P*4*mm* + *R*3*c* model: $\chi^2 = 3.926$, $R_{wp} = 7.98\%$, $R_{wpb} = 7.21\%$, $R_p = 9.36\%$, and $R_{pb} = 10.15\%$.

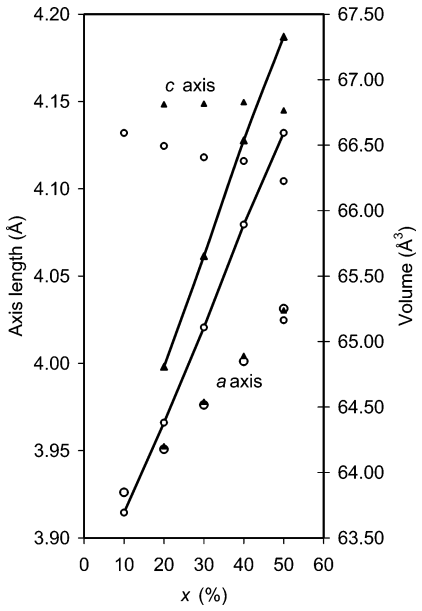

Figure 3. Room-temperature lattice parameters for PHT (circles) and PZT ceramics (triangles). Also the primitive cell volume is indicated, circles connected by a line and triangles connected by a line correspond to the PHT and PZT volumes, respectively. The data for PZT ceramics was adapted from ref 18. In the case of the PHT sample with $x = 0.50$, the monoclinic *a* and *b* axes lengths were divided by $\sqrt{2}$ to allow for an easier comparison with the tetragonal *a* axis length.

reflections. Anisotropic line broadening was also observed in PZT powders. Earlier studies of PZT indicated that the Pb ions are shifted toward four ⟨110⟩ directions, which was subsequently assumed to explain the diffuse scattering component observed between the tetragonal 200 and 002 reflections.[2] In this work, it is interesting to note that the intensity between the tetragonal 220 and 202 reflections increases with increasing *x* (Figure 4). It is clear that two sharp and strong peaks, belonging to the rhombohedral phase, are developed within this region, in addition to the four monoclinic reflections. This fits with the idea, previously proposed for the PZT system,[2] that the *Cm* phase serves as a transitional phase between the tetragonal and rhombohedral phases. Our present data (see Table 1) indicate that the Pb ion displacements are of the same order as those of the PZT ceramics,[18] but the peak-broadening behavior is quite different. The diffuse scattering, shown in Figure 4, could be assigned to Pb ion displacements, as it corresponds to the intensity between reciprocal lattice vectors. It is also consistent with the observation that the Pb ion displacements increase with increasing *x*. The problem of Bragg peak broadening is not trivial, as it is necessary to consider substitutional disorder at the B cation site and displacement disorder at the B cation site, which is accompanied by variations in the *c* axis length. Displacement disorder can be further divided into static and dynamic cases. Substitutional and displacement disorder often occur simultaneously, as is believed to be true in the present case. The origin of displacement disorder relies on the fact that the ionic radii of Hf^{4+} and Ti^{4+} are different. In addition, one should consider different B cation combinations, such as the Ti ion having Ti ions as its nearest B cation neighbors. As discussed below, the net result was combined under a single concept of "spatial-composition fluctuation", which causes reflection index-dependent line broadening. For the following discussion, dedicated to the Ti-rich PHT solid solutions and to the qualitative understanding of the intensity behavior of the *h*00 and 00*l* reflections, we assumed that the substitutional disorder at the B cation site is perfect (an underlying assumption of the present Rietveld refinement). This allows computation of the average structure factor by further assuming that the lattice is tetragonal. Our approach was to analyze the structure factors and fwhm values of the *h*00 and 00*l* reflections to exclude certain types of disorder mechanism.

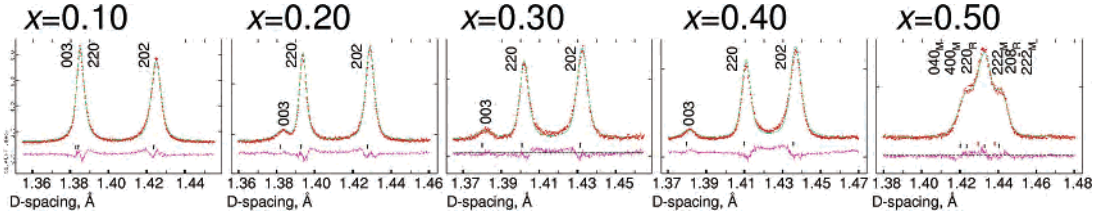

Figure 4. Tetragonal 220 and 202 reflections ($0.10 \le x \le 0.40$ data). Note the increasing intensity between these two peaks with increasing *x* and the formation of rhombohedral peaks within this region. In the case of the $x = 0.50$ data, labels R and M were used to indicate reflections which were characteristic to the *R*3*c* and *Cm* phases, respectively. The upper and lower tick marks ($x = 0.50$ data) correspond to the *R*3*c* and *Cm* phases, respectively.

Table 3. F_O^2 and F_C^2 Values (on an absolute scale) of the Pseudo-Cubic *h*00 and 00*l* Reflections for the PHT Samples[a]

		200		002		300		003		400		004		500		005	
x	*T* (K)	F_O^2	F_C^2	F_O^2	F_C^2	F_O^2	F_C^2	F_O^2	F_C^2	F_O^2	F_C^2	F_O^2	F_C^2	F_O^2	F_C^2	F_O^2	F_C^2
0.10	4	5.55	5.51	3.61	3.16	0.34	0.33	2.23	2.39	4.32	4.27	0.70	0.46	0.28	0.29	1.39	2.02
0.10	295	5.18	5.17	3.70	3.34	0.25	0.24	1.68	1.89	3.53	3.28	0.57	0.53	0.12	0.12	1.15	1.52
0.20	4	5.70	5.73	3.91	3.43	0.18	0.20	1.73	2.12	4.06	3.78	0.61	0.31	0.14	0.14	0.81	1.59
0.20	295	5.38	5.38	3.93	3.65	0.15	0.15	1.43	1.67	3.28	3.08	0.53	0.52	0.05	0.05	0.79	1.18
0.30	4	6.31	6.31	4.57	3.93	0.08	0.12	1.82	2.15	4.81	4.31	0.90	0.35	0.08	0.08	0.64	1.80
0.30	295	4.97	4.88	3.68	3.46	0.04	0.05	1.13	1.34	2.71	2.58	0.75	0.50	0.00	0.00	0.72	0.89
0.40	4	6.61	6.71	4.70	4.42	0.04	0.05	1.65	2.08	4.37	4.28	0.61	0.39	0.02	0.02	1.30	1.61
0.40	295	5.87	6.01	4.57	4.43	0.02	0.02	1.14	1.33	2.93	2.76	0.63	0.62	0.00	0.00	0.84	0.81
0.50	2	30.22	29.82	21.92	21.46	0.60	1.12	6.03	7.72	22.96	20.88	7.35	4.60	2.24	1.92	6.73	7.03
0.50	280	29.33	29.40	22.41	21.91	0.19	0.57	4.36	6.28	21.47	18.79	9.01	5.02	1.04	0.89	4.88	5.28

[a] The values for $x = 0.50$ correspond to the *Cm* phase.

3.1.1. The Intensities of the *h*00 and 00*l* Reflections. The average structure factor, F_{hkl} (assuming the same atomic displacement parameter U_{iso}(B) for Hf and Ti), for the tetragonal model used in the present study is

$$F_{hkl} = (b_{Pb}/2)\{\cos[2\pi(h+k)x(\mathrm{Pb})] + \cos[2\pi(h-k)x(\mathrm{Pb})]\} \exp[-2\pi^2 U_{iso}(\mathrm{Pb})/d^2] + \{x b_{Hf} \exp\{i\pi[h+k+2lz(\mathrm{Hf})]\} + (1-x) b_{Ti} \exp\{i\pi[h+k+2lz(\mathrm{Ti})]\}\} \exp[-2\pi^2 U_{iso}(B)/d^2] + b_O\{\exp[i\pi(h+k+2lz(\mathrm{O}_1))] + \exp[i\pi(h+2lz(\mathrm{O}_{2,3}))] + \exp[i\pi(k+2lz(\mathrm{O}_{2,3}))]\} \exp[-2\pi^2 U_{iso}(\mathrm{O})/d^2]$$

where b_{Pb}, b_{Hf}, b_{Ti}, and b_O are the neutron scattering lengths for Pb, Hf, Ti, and O, respectively. Thus, each primitive cell was assumed to scatter neutrons in an identical way by introducing "fractional B cations". Although this is not strictly valid (a more accurate approach would be to relax the constraint set by translational symmetry and allow each primitive cell to have different scattering power, which depends on the composition and structure of the primitive cell), it is sufficient to reveal the nature of the disorder present.

Table 3 compares the squared absolute values of the observed structure factors, (abbreviated as F_O^2) to the squared absolute values of the calculated structure factors F_C^2. To compare these values with the observed intensities, corrections for the reflection multiplicity and the Lorentz factor are necessary. Although the F_O^2 values are biased by the structural model used, meaningful comparison is achieved for the 200, 002, 300, 003, 400, 004, 500, and 005 reflections, as they overlap at most with one reflection (see Figure 1). As Table 3 reveals, the F_O^2 values for the even and odd 00*l* reflections were larger and smaller than the F_C^2 values, respectively, and this feature was more pronounced at low temperature (the 005 reflection observed at 295 K in the $x = 0.40$ sample was an exception). The index dependence of the *h*00 reflections was not so clear. The F_O^2 and F_C^2 values for *h*00 were similar, although $F_O^2 > F_C^2$ for the 400 reflections. These features hint that the origin of the intensity behavior is disorder occurring along the *c* axis: because of the short *a* axis length, hafnium ions are forced into different positions than titanium ions, which results in a spatial variation in the *c* axis length and is mainly related to the B cation displacement disorder. The slightly larger atomic displacement parameter value of O_1 in the case of the $x \leq 0.30$ samples at low temperature is consistent with this. Figure 5 illustrates the type of disorder assumed to be responsible for the observed features. However, with increasing *x*, one should also relax the constraint that the nearest neighbor distance between these rows is constant. This assumption was based on the fact that the fwhm values of the *l*00 and 00*l* reflections became comparable to each other and that the symmetry was decreased to *Cm*. The disorder shown in Figure 5 was partially taken into account by allowing the fractional *z* coordinates of the Hf and Ti ions to differ. The next goal is to compare the lattice parameter data given in Tables 1 and 2 and Figure 3 and to seek an explanation which is consistent with the observed peak intensities and widths and lattice parameters versus *x*.

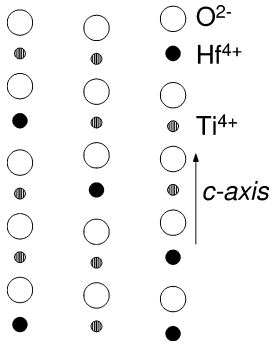

Figure 5. Schematic picture showing the combined effect of displacement and substitutional disorder which was assumed to be responsible for the observed Bragg reflection peak intensity and anisotropic broadening behavior. For small values of *x*, it was assumed that these rows are parallel (as required by the tetragonal symmetry) and that the rows were almost equidistantly distributed.

3.1.2. fwhm Behavior of the h00 and 00l Reflections. Microstrain parameters are listed in Tables 4 and 5. Figure 6 shows the fwhm values of the tetragonal *h*00 and 00*l* and monoclinic *hh*0 and 00*l* reflections. The fwhm values decrease with increasing reflection index *h* and *l*, as eq 1 implies. The essential point is that this line shape was able to give a good fit for all reflections. We note that the $\sigma_1^2 d^2$ term had a minor effect on the fwhm values, consistent with the expectation that line-broadening mechanisms originating from the sample dominate in the present case.

The observed line broadening is qualitatively consistent with the idea of a spatial composition variation, since the line broadening should become narrower with increasing reflection index. If the spatial composition variation δx

Table 4. Microstrain Parameters for the $0.10 \leq x \leq 0.40$ Samples[a]

x	0.10	0.10	0.20	0.20	0.30	0.30	0.40	0.40
T (K)	4	295	4	295	4	295	4	295
η	0.7493(27)	0.7424(27)	0.7080(32)	0.7003(30)	0.6852(40)	0.7020(35)	0.7002(38)	0.7065(37)
S_{400}	79.39(64)	72.95(60)	61.79(59)	55.22(52)	100.8(11)	90.32(95)	103.3(11)	94.3(10)
S_{004}	377(3)	365(3)	207(3)	176(2)	263(5)	231(3)	231(4)	197(3)
S_{220}	40(1)	35(1)	33(1)	28(1)	57(1)	48(2)	57(2)	47(2)
S_{202}	8(1)	−10(1)	16(1)	2(1)	36(1)	10(1)	59(1)	17(1)

[a] The other profile parameters were the instrument parameters $\alpha = 0.1624$, $\beta_0 = 0.02654$, $\beta_1 = 0.09735$, and $\sigma_1^2 = 225$, which were kept fixed during the refinement.

Table 5. Microstrain Parameters for the $x = 0.50$ Sample[a]

T (K)	2	2	50	50	140	140	280	280
space group	Cm	*R*3*c*	Cm	*R*3*c*	Cm	*R*3*c*	Cm	*R*3*c*
η	0.387(14)	0	0.387(12)	0	0.377(15)	0	0.390(14)	0
S_{400}	23(1)	14.0(55)	23(1)	13.84(51)	20(1)	13.20(54)	18(1)	11.8(4)
S_{040}	35(1)		35(1)		31(1)		30(1)	
S_{004}	312(10)	0.170(14)	312(9)	0.183(14)	270(10)	0.152(14)	234(8)	0.161(14)
S_{220}	36(1)		37(1)		34(1)		28(1)	
S_{202}	−25(2)	11.69(34)	−26(2)	11.18(31)	−21(2)	11.11(34)	−17(1)	9.61(26)
S_{022}	−41(2)		−41(2)		−36(2)		−32(2)	
S_{301}	−33(2)	0	−32(1)	0	−32(2)	0	−31(1)	0
S_{103}	87(4)		87(4)		89(4)		84(4)	
S_{121}	−25(1)		−25(1)		−26(2)		−26(1)	

[a] The other profile parameters were the instrument parameters $\alpha = 1.456$, $\beta_0 = 0.02647$, $\beta_1 = 0.01073$, and $\sigma_1^2 = 209.1$, which were kept fixed during the refinement.

corresponds to the lattice parameter variations δa and δc, the line broadening of the $h00$ and $00l$ reflections should decrease linearly with increasing indices h and l. Although this discussion provides a qualitative idea, an inspection of Tables 1 and 2 reveals that at low temperature $\Delta a/\Delta x \approx -7\Delta c/\Delta x$. Thus, it is clear that the effect of spatial composition variation cannot be estimated from the dependence of lattice parameters on x (as it predicts that the $h00$ reflections should be significantly larger than the $00l$ reflections). This is particularly true for small values of x: Hf ions produce local distortions, which mainly result in a change in the c axis length, and to a lesser extent, a change in the a axis length. This is also consistent with the intensity behavior given above. One expects that the microstrain caused by the Hf substitution for Ti should be most clearly seen in the case of the smallest primitive cell volumes. As shown in Figure 6, the difference between the fwhm values of the $h00$ and $00l$ reflection pairs decreases with increasing x.

It is also of interest to determine if the tabulated S_{HKL} values obey the redundancy relations given in ref 19. In the following discussion, we use the GSAS convention for the S_{HKL} parameters which, in the case of some parameters, differ from the Stephens definitions by a constant prefactor (see Table 3 in ref 19). For the tetragonal crystal system, the relationships $3S_{220} = 2S_{400}$ and $3S_{202} = \pm 2\sqrt{S_{400}S_{004}}$ hold (two parameters suffice, instead of the four used in the present case) and for the monoclinic crystal system S_{220}, S_{202}, S_{022}, S_{301}, and S_{121} can be expressed in terms of S_{400}, S_{040}, S_{004}, and S_{103}: $3S_{220} = \pm 2\sqrt{S_{400}S_{040}}$, $3S_{202} = \pm 2\sqrt{S_{400}S_{004}} + S_{103}^2/S_{004}$, $3S_{022} = \pm 2\sqrt{S_{040}S_{004}}$, $S_{301} = \pm 2\sqrt{S_{400}/S_{004}}S_{103}$, and $3S_{121} = \pm 2\sqrt{S_{040}/S_{004}}S_{103}$. As can be seen using the values from Tables 4 and 5, these relationships are not obeyed. This is plausible since the composition variation, even if dominant, results in accompanying hkl-dependent line-broadening effects. One could also speculate that the role of strain in domain or grain boundaries should contribute to the line broadening, while the line shape used also absorbs the effect of diffuse scattering (i.e., caused by the Pb ions displaced from their ideal positions). However, it is clearly not possible to test all alternative line-broadening models. Nevertheless, meaningful refinements and structural parameters (as tested by computing bond-valence sums and polarization values) could be obtained using the approach described here.

3.1.3. Comparison to the Previous Studies. Raman scattering experiments showed that the frequency of the A_1 symmetry modes (in which ions move along the c axis direction) were larger in the case of PHT ceramics than in the case of PZT ceramics.[10] This is somewhat puzzling as the significantly larger average B cation mass tends to decrease the vibration frequencies. A partial explanation can be found if one notes that the c axis length (and average bond lengths) is shorter in the case of PHT ceramics. The second interesting feature is that the c axis length in PZT ceramics was almost constant in the tetragonal regime, while it decreases with increasing x in the case of PHT ceramics. The behavior of the c axis is directly related to the piezoelectric response of these materials: in tetragonal PZT ceramics, the c axis decreases rapidly once the composition approaches the MPB compositions. Interestingly, the same behavior was observed in PZT with $x = 0.40$ under the influence of high pressure.[6] A more detailed discussion related to the bond length changes in the case of PZT samples is given in ref 12. The two main structural changes versus composition are (i) a shear of the oxygen planes approximately perpendicular to the pseudocubic [111] direction and (ii) an increase in the distance between the oxygen planes. In addition, tilts of these planes and an adjustment of the oxygen bond lengths occur. Very similar changes occur versus pressure: in the case of PZT with $x = 0.40$ the room

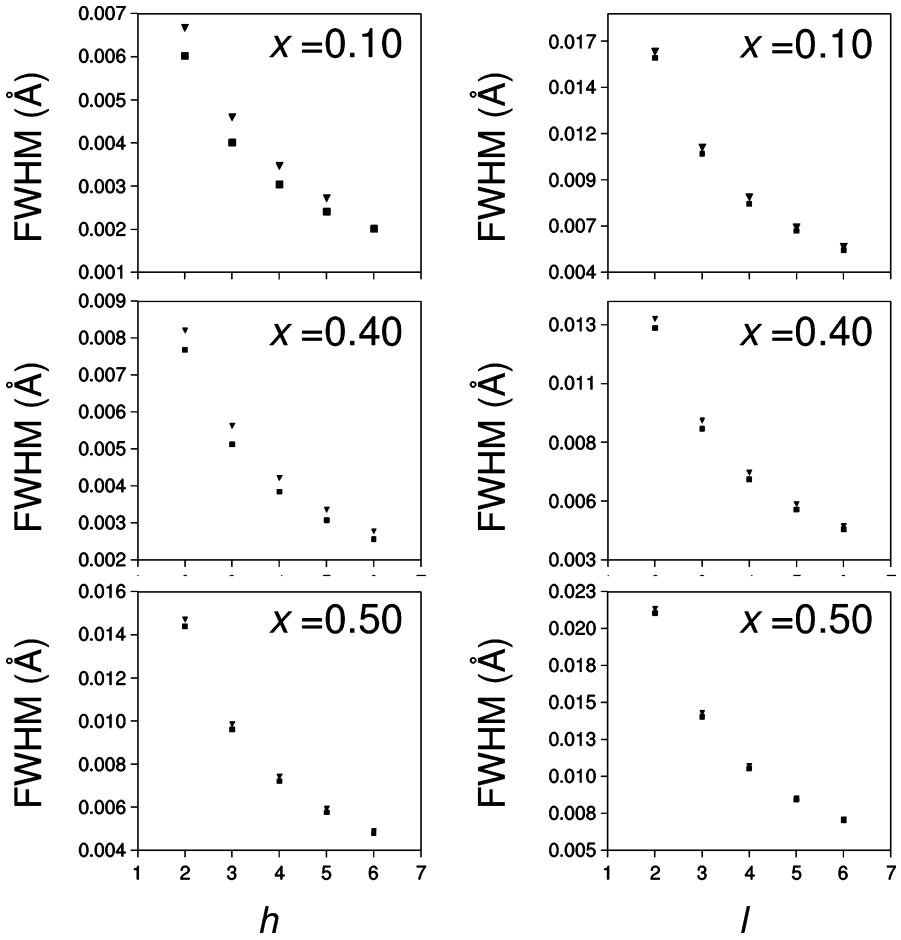

Figure 6. fwhm values obtained through the Rietveld refinement carried out for the data collected at 2 K from the $x = 0.10$, 0.40 (*P*4*mm* phase), and 0.50 (*Cm* phase) samples. Left and right panels show the fwhm values for the *h*00 and 00*l* reflections (*P*4*mm* symmetry) or *hh*0 and 00*l* reflections (*Cm* symmetry). The fwhm values decrease with *h* and *l*. Filled triangles are the fwhm values obtained through eq 1 by setting $\sigma_1 = 0$, whereas the filled squares are the observed fwhm values (and include the instrumental contribution). The key point is that this type of line shape refined the data well and thus provided further evidence that the index dependent line broadening is predominantly the result of the spatial composition variation.

Table 6. Magnitude of the Spontaneous Polarization, P_S, Estimated from the Data Given in Tables 1 and 2[a]

T (K)	295	4	295	4	295	4	295	2	280	280	140	140	50	50	4	4
x	0.10	0.10	0.20	0.20	0.30	0.30	0.40	0.40	0.50	0.50	0.50	0.50	0.50	0.50	0.50	0.50
space group	*P*4*mm*	*P*4*mm*	*P*4*mm*	*P*4*mm*	*P*4*mm*	*P*4*mm*	*P*4*mm*	*P*4*mm*	*Cm*	*R*3*c*	*Cm*	*R*3*c*	*Cm*	*R*3*c*	*Cm*	*R*3*c*
P_S (μC cm^{-2})	52.9	55.5	52.3	54.2	45.6	45.6	29.1	45.4	36.3	35.9	38.3	35.0	38.6	38.5	39.0	38.3
$P_{S,x}$ (μC cm^{-2})									−10.8		−12.0		−13.0		−13.8	
$P_{S,z}$ (μC cm^{-2})									34.6		36.3		36.2		36.3	
θ (deg)									17.6		18.6		20.2		21.2	
θ_R (deg)									54.2		54.2		54.2		54.2	

[a] In the case of *Cm* symmetry, P_S lies in the *ac* plane and thus has two components. The θ angle is the angle between the normal to the *ab* plane and $\mathbf{P}_S$ and is compared to the angle $\theta_R = \arccos(c/\sqrt{a^2+c^2})$. The spontaneous polarization values for the *R*3*c* phase, especially those corresponding to room temperature, should be treated with caution, see text.

temperature (and atmospheric pressure) tetragonal lattice parameters were $a = 4.004298$ Å and $c = 4.14964$ Å,[18] whereas the monoclinic lattice parameters were reported to be $a = 5.6441(2)$ Å, $b = 5.6425(2)$ Å, $c = 4.0828(2)$ Å, and $\beta = 90.109(12)°$ at 2.7 GPa.[6] It can be seen that, despite the large pressure, there is almost no change in lattice parameters perpendicular to the *c* axis ($a/\sqrt{2} = 3.9910$ Å and $b/\sqrt{2} = 3.9895$ Å), whereas the *c* axis itself is drastically reduced.

The structural data given in Tables 1 and 2 allowed us to estimate the spontaneous polarization values, $\mathbf{P}_S$, tabulated in Table 6. Unlike the cases of the *P*4*mm* and *R*3*c* symmetries (where $\mathbf{P}_S$ is along the unique axis), *Cm* symmetry allows the direction of the $\mathbf{P}_S$ to point any direction in the *ac* plane. Correspondingly, for *Cm* symmetry the direction angle θ (the angle between $\mathbf{P}_S$ and the *ab* plane normal) is also given. For consistency, the $\mathbf{P}_S$ values were also given for the *R*3*c* phase, although they should be treated with caution (the most reliable $\mathbf{P}_S$ value corresponds to 2 K). Table 6 shows two features: the magnitude of $\mathbf{P}_S$ decreases with increasing *x* and increases with decreasing temperature. The *Cm* data show that θ increases with decreasing temperature. This is mainly the result of the increase in $P_{S,x}$. The general tendency was that the $\mathbf{P}_S$ value decreases with increasing *x*. Similar behavior was observed in the case of PZT ceramics.[18] The electrical measurements

Table 7. Valences of Ions Estimated by Applying the Bond-Valence Method to the NPD Data[a]

T (K)	295	4	295	4	295	4	295	4	280	280	140	140	50	50	4	4
x	0.10	0.10	0.20	0.20	0.30	0.30	0.40	0.40	0.50	0.50	0.50	0.50	0.50	0.50	0.50	0.50
space group	*P4mm*	*P4mm*	*P4mm*	*P4mm*	*P4mm*	*P4mm*	*P4mm*	*P4mm*	*Cm*	*R3c*	*Cm*	*R3c*	*Cm*	*R3c*	*Cm*	*R3c*
υ(Pb)	2.01	2.11	1.95	2.05	1.88	1,992.02	1.81	1.92	1.92	1.88	2.00	1.92	2.05	1.87	2.06	1.99
	2.04	2.13	1.98	2.08	1.93		1.85	1.97								
υ(Hf)	5.58	5.57	5.42	5.39	5.19	5.15	5.02	5.13	4.92	4.83	4.93	4.80	4.93	4.80	4.93	4.75
υ(Ti)	3.81	3.75	3.74	3.71	3.61	3.55	3.44	3.59	3.38	3.32	3.38	3.29	3.38	3.30	3.39	3.26
υ(B$_{av}$)	3.98	3.93	4.08	4.05	4.08	4.03	4.07	4.21	4.15	4.07	4.16	4.05	4.16	4.05	4.16	4.00
Hf−O−Hf																
υ(O$_1$)	2.51	2.47	2.44	2.37	2.22	2.13	2.05	2.15	2.24		2.28		2.29		2.29	
υ(O$_{2,3}$)	2.54	2.60	2.47	2.54	2.43	2.51	2.39	2.45	2.30	2.24	2.32	2.24	2.35	2.22	2.35	2.24
Hf−O−Ti																
υ(O$_1$)	2.41	2.40	2.31	2.24	2.04	1.94	2.04	1.95	2.06		2.10		2.12		2.11	
υ(O$_{2,3}$)	2.26	2.32	2.18	2.25	2.14	2.22	2.14	2.17	2.05	2.12	2.08	2.07	2.09	2.11	2.11	2.11
Ti−O−Hf																
υ(O$_1$)	1.97	1.86	2.02	1.97	1.97	1.87	1.78	1.92	1.91		1.95		1.97		1.97	
υ(O$_{2,3}$)	2.26	2.32	2.18	2.25	2.14	2.22	2.12	2.17	2.03	1.85	2.05	1.91	2.07	1.84	2.07	1.88
Ti−O−Ti																
υ(O$_1$)	1.87	1.84	1.89	1.84	1.78	1.69	1.59	1.73	1.73		1.78		1.79		1.79	
υ(O$_{2,3}$)	1.97	1.96	1.90	1.96	1.85	1.93	1.84	1.90	1.78	1.73	1.80	1.74	1.82	1.72	1.83	1.75
υ(O$_{1av}$)	1.93	1.95	2.00	1.95	1.91	1.92	1.76	1.89	1.99		2.03		2.04		2.04	
υ(O$_{2,3av}$)	2.03	2.07	2.01	2.08	2.03	2.10	2.06	2.12	2.04	1.98	2.07	1.99	2.08	1.97	2.09	2.00
υ(O$_{av}$)	2.00	2.03	2.01	2.03	1.99	2.01	1.96	2.04	2.02	1.98	2.05	1.99	2.07	1.97	2.07	2.00
$\sum_i \upsilon_i$	0.00	0.00	0.00	0.00	0.00	0.00	0.00	0.00	0.00	0.00	0.00	0.00	0.00	0.00	0.00	0.00

[a] An average for the B cations is also given, where $\upsilon(B_{av}) = x\upsilon(Hf) + (1 - x)\upsilon(Ti)$. Nominal valences (as indicated in the second row) were used. The length of the line between oxygen and the cation (Hf or Ti) indicates the bond lengths. In the case of space groups *P4mm* and *Cm*, the average oxygen valence was $\upsilon(O_{av}) = {}^1/_3\upsilon(O_{1av}) + {}^2/_3\upsilon(O_{2,3av})$.

typically give slightly larger $\mathbf{P}_S$ values than estimations based on atomic positions. The latter estimation neglects the electric polarization, which in principle could be taken into account by constructing the electron density maps based on X-ray diffraction data. There are two often quoted values of $\mathbf{P}_S$ for $PbTiO_3$, 56 μCcm^{-2} [28] and 75 μCcm^{-2}.[29] In practice the $\mathbf{P}_S$ values can be estimated from the ferroelectric hysteresis loops measured from the poled ceramics, although the shape of the loop does have an effect on the estimated $\mathbf{P}_S$ values. Correspondingly, it is rather common to see that remanent polarization P_r, instead of the $\mathbf{P}_S$, reported. In the case of the PZT ceramics, the P_r values were found to have a maximum at $x = 0.54$ [30] or at $x = 0.52$ [31] for $0.40 \le x \le 0.60$. However, the dependence of P_r on x is not very clear, but the maximum value, 36 $\mu C\ cm^{-2}$ [31] compares to our estimations for the $x = 0.50$ PHT and PZT samples.

3.2. Bond-Valence Calculations. Bond-valence calculations were carried out to test the reliability of the refinement results. Temperature corrections (correction for the change in bond lengths) for the ion pair specific constants were carried out separately for each phase. Room-temperature values of these constants for each of the ion pairs were adapted from ref 32. Table 7 shows the estimated valences for each ion.

The general features are the same as those found in the case of PZT ceramics. Oxygen valences were close to the nominal ones, while the valences of the Pb and B cation were smaller and larger than the nominal ones, respectively. The Pb ion and average B cation valences tend to decrease and increase with increasing x, respectively. This behavior can be understood by noting that the cuboctahedral volume increases with increasing x, whereas the increase in oxygen octahedral volume was not sufficient to compensate for the larger number of short Hf−O bond lengths. Once the symmetry is changed to monoclinic, the Pb ion bond valence is almost the nominal one because Pb ions are coherently shifted toward the pseudocubic 110 direction. Present bond valence data are consistent with the notion that the oxygen octahedra can be approximated as a rigid network, where the cations attempt to adjust their positions in such a way that their nominal valences are achieved.

4. Conclusions

High-resolution time-of-flight neutron powder diffraction data were collected on lead hafnate titanate (PHT) samples and analyzed using Rietveld refinement. Titanium rich samples were tetragonal (space group *P4mm*), while the symmetry of the $x = 0.50$ sample was predominantly monoclinic (space group *Cm*). As this sample had a composition close to the phase boundary, it also contained a minor phase modeled by rhombohedral symmetry *R3c*. The low-temperature phase transition, previously revealed by Raman scattering technique to occur in the x range from 0.40 to 0.50, was confirmed. The overall structural features (phase-transition sequences and lattice parameters) were similar to those observed in lead zirconate titanate (PZT) ceramics. For the same value of x, the tetragonal c axis and primitive cell volume of PHT ceramics were smaller than those of PZT ceramics, while the a axis lengths were almost identical. The Pb ion displacements toward ⟨110⟩ directions had a similar

(28) Remeika, J. P.; Glass, A. M. *Mater. Res. Bull.* **1970**, *5*, 37.
(29) Gavrilyachenko, V. G.; Pinko, R. I.; Martynenko, M. A.; Fesenko, E. G. *Sov. Phys. Solid State* **1970**, *125*, 1203.
(30) Jaffe, B.; Cook, W. R.; Jaffe, H. *Piezoelectric Ceramics*; Academic Press: New York, 1971.
(31) Chen, H. D.; Udayakumar, K. R.; Gaskey, C. J.; Cross, L. E. *Appl. Phys. Lett.* **1995**, *67*, 3411.
(32) Rohrer, G. S. *Structure and Bonding in Crystalline Materials*; Cambridge University Press: Cambridge, U.K., 2001.

order of magnitude in PHT and PZT systems. The diffuse scattering, seen as an increased intensity between Bragg reflections, was assigned to Pb ion displacements. Structural disorder occurring along the *c* axis in PHT samples, including the $x = 0.50$ sample, was observed. This was observed as the pseudo-cubic 00*l* peaks being broader than the *h*00 peaks. The observed intensities of the 00*l* reflections with *l* even and odd were smaller and larger, respectively, than those corresponding to the refined model. The intensity and peak width behavior was attributed to the disorder of the O−B−O chains parallel to the *c* axis. For small values of *x*, this shift was dominantly along the *c* axis, whereas shifts perpendicular to the *c* axis increased with increasing *x*. In addition, the *c* axis decreases with increasing *x* faster in the case of PHT than in the case of PZT crystals. The overall importance of correct profile function for structure refinement and for the symmetry assignment was addressed.

Acknowledgment. This work was supported by the Academy of Finland (Project Numbers 207071 and 207501) and the Japan Society for the Promotion of Science.

IC051169M